Chemical and steric effects in simulating noncontact atomic force microscopy images of organic molecules on a Cu (111) substrate

Dingxin Fan [1], Yuki Sakai,[2] and James R. Chelikowsky [1,2,3,*]

[1]*McKetta Department of Chemical Engineering, The University of Texas at Austin, Austin, Texas 78712, USA*
[2]*Center for Computational Materials, Oden Institute for Computational Engineering and Sciences, The University of Texas at Austin, Austin, Texas 78712, USA*
[3]*Department of Physics, The University of Texas at Austin, Austin, Texas 78712, USA*

(Received 14 November 2019; revised manuscript received 20 February 2020; accepted 15 April 2020; published 27 May 2020; corrected 7 June 2021)

Noncontact mode of atomic force microscopy (nc-AFM) employing a CO-functionalized tip is a very powerful tool for studying molecular structures. However, interpreting nc-AFM images for nonplanar molecules can sometimes be problematic. To illustrate and resolve the nature of such problematic systems, we employ real-space pseudopotentials constructed within density functional theory to simulate nc-AFM images. We focus on several representative nonplanar organic molecules (pentacene, naphthanthrone, olympicene, and 6-phenylhexa-1,3,5-triynybenzene (PHTB)) on a typical substrate: the Cu (111) surface. This substrate results in significant distortions in the molecular geometries of pentacene and naphthanthrone. Including these distortions in simulated nc-AFM imaging notably improves the agreement between the simulated and measured images. In naphthanthrone, the relatively large interaction between the O atom and the Cu substrate offers a straightforward explanation for the absence of the C = O bond in the measured image. Nonplanar features such as tilting or twisting are also apparent in olympicene and PHTB. A "triangular" bright feature associated with the $-CH_2$ group in olympicene appears in simulated and measured nc-AFM images. This feature is directly related to the tilting angle of the molecule with respect to the Cu substrate. The "defective" benzene ring feature and the faint ellipsoidal C ≡ C feature in PHTB can be ascribed to its twisted nature. The ability to simulate such subatomic images in nc-AFM reflects the accuracy and efficiency of calculating quantum forces in real space.

DOI: 10.1103/PhysRevMaterials.4.053802

In 1986, Binnig, Quate, and Gerber invented atomic force microscopy (AFM) [1]. A primary motivation of their work was to overcome a limitation of the scanning tunneling microscopy (STM). Namely, STM works best when the sample is conducting so that electrons can tunnel into or out of the sample. This often restricts STM to metals or semiconductors. In contrast, AFM generates an image by measuring the force on a probe tip exerted by the sample. Since a conducting sample is not required, AFM can readily be used to image ceramics, polymers, plastics and organic materials.

There are several different operation modes of AFM. Here, we focus on the noncontact mode (nc-AFM), which employs a probe tip oscillating at a resonant frequency. nc-AFM is commonly used for characterizing subatomic features on molecular scale [2–5]. In particular, changes from the resonant frequency in the oscillating tip are measured as the probe tip scans the specimen at a constant height (frequency modulation mode).

In 2009, Gross *et al.* demonstrated that subatomic resolution with this nc-AFM mode was possible [6]. They achieved unprecedented atomic resolution images of pentacene wherein C-C covalent bonds were clearly resolved. A probe tip functionalized with a CO molecule was a key aspect of their nc-AFM setup. Recently, this technique has been used to study surface microstructures and molecular structures for a variety of systems [7–33].

Modeling such systems can be difficult. In principle, the tip, the specimen, and the substrate need to be included. Theoretical simulations with functionalized tips have been employed to interpret interesting features in experimental nc-AFM images [34–47]. Even though nc-AFM with a CO tip has achieved extraordinary success in terms of molecular identification, characterizing nonplanar organic molecules remains a challenge.

In this paper, we employ a real-space pseudopotential density functional theory (DFT) [48,49] code, PARSEC [50–55], to simulate nc-AFM images of the following representative molecules with a model CO probe tip: (1) pentacene, (2) naphthanthrone, (3) olympicene, and (4) 6-phenylhexa-1,3,5-triynylbenzene (PHTB). We choose these molecules owing to anomalies in the measured nc-AFM images. In particular, (1) previous simulations for pentacene does not account for the presence of stretched benzene rings; (2) the C = O bond in naphthanthrone is not experimentally reproduced; (3) the $-CH_2$ group in olympicene appears as a bright triangular feature; and (4) C ≡ C bonds appear quite different when compared to single and double bonds, i.e., they appear as fainter bright spots comparing with the brightness of the "defective" benzene rings.

*jrc@utexas.edu

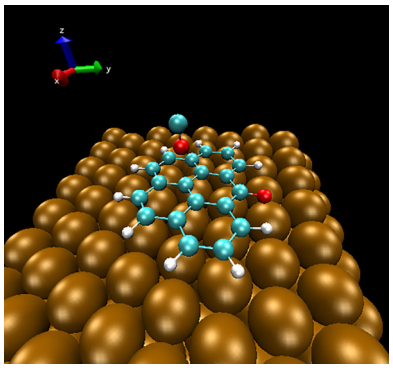

FIG. 1. Schematic view of a simulated system: naphthanthrone molecule at an hcp30° adsorption site on a Cu (111) surface. A CO tip is placed above the sample molecule. Brown: Cu, blue: C, red: O, and white: H.

Figure 1 shows a schematic view of our model for nc-AFM simulation. We model the functionalized tip with only a single CO molecule as previous studies using CO bonded to a metal tip apex have shown that this simplification gives accurate results [34–36].

We generate 2D uniform grids (in the $x-y$ plane) for the moving CO tip over the sample molecule and compute the total energy of the tip-sample system ($E_{\rm ts}$) at each grid point. We assume the movement of the tip in the frequency modulation nc-AFM is harmonic and the tip oscillation amplitude is small [56,57] so that the relative frequency shift (Δf) can be computed from total energy calculations by using finite differences:

$$\Delta f = \frac{\partial^2 E_{\rm ts}}{\partial z^2} = \frac{E_{-1} - 2E_0 + E_1}{h^2}, \tag{1}$$

where E_{-1}, E_0, and E_1 correspond to the total energy of the tip-sample system at three different heights for each lateral grid point and h is the separation distance between two neighboring vertical grid points.

For the total electronic energy calculations performed, we incorporate Troullier-Martin norm-conserving pseudopotentials [58] and the local density approximation by Ceperley-Alder (without spin polarization) for the exchange-correlation functional [59,60]. We solve the Kohn-Sham equation in real space within a spherical domain. The grid spacing of the real-space cubic grid (for electronic structure calculations) is set to be 0.30 a.u. (1 a.u. $= 0.5292$ Å). The grid size for rendering the simulated integers in the $x-y$ plane (Fig. 1) is set to be an integer multiple of the grid spacing.

We optimize the molecular structures imaged in the nc-AFM simulations. We then fix the atomic geometry of the samples in AFM simulations as the tip-sample interaction is not strong at relatively large tip heights (above 5.0 a.u.). For pentacene and naphthanthrone, we investigate the role of the substrate on nc-AFM images by relaxing each specimen at certain adsorption sites on Cu (111) surfaces. We model the substrate using an 8×4 (eight Cu atoms in the direction of the long axis) and an 8×8 four-layered Cu (111) surfaces supercell for pentacene and naphthanthrone respectively. In both cases, we fully relax the top two layers. We use a 2D confined boundary condition, which assumes the system is

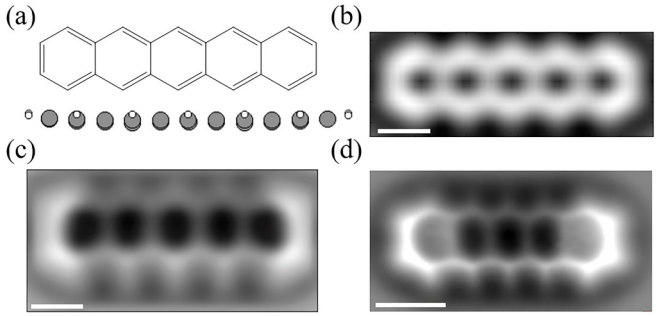

FIG. 2. (a) Kekulé structure and a side view of the relaxed (bent) structure of pentacene. Gray: C, white: H. [(b) and (c)] Simulated nc-AFM image of pentacene on Cu (111) before (b) and after (c) structural relaxation. Tip height is 5.8 a.u. and the lateral spring constant of CO tip is 0.24 N/m. (d) Experimental nc-AFM image of pentacene on a Cu (111) substrate. The scale bars correspond to 5 a.u. in (b) and (c) and correspond to 9.45 a.u. in (d). (b) is adapted from Ref. [36]. (d) is adapted from Ref. [6].

periodic along the Cartesian x and y directions, for molecule on metal surface systems. We consider only the relaxed structures when simulating the images and directly exclude the Cu layers when running AFM calculations. We find explicitly including the substrate has a negligible contribution to AFM calculations [36].

To minimize the computational load, we employ the frozen density embedding theory (FDET) [37,61]. With FDET, we divide the total charge density of a system into two subsystems: (1) tip and (2) sample. FDET calculations for the tip are performed following a full DFT run of the sample system and using the Hartree potential, nuclear potential, and the charge density of the sample system as inputs. This theory accurately reproduces full-DFT results by adjusting the simulation tip height by approximately 0.6 a.u. [37].

Our previous work has shown that the flexibility of the CO molecule with respect to lateral forces can strongly affect the resulting nc-AFM images [34,37,38]. To account for the tip relaxation effect, we use a tip tilting correction for the lateral force proposed by Guo *et al.* [62,63]. With this correction, we first compute the lateral forces in x and y directions, $\vec{F}_{\rm lat}(x, y)$, using the total energies of the neighboring lateral grid points in the middle energy plane by a finite difference method. We compute the displacement of O atom in x and y directions, $\vec{\Delta}_{\rm lat}(x, y)$, by assuming a linear relationship between the lateral force and the lateral displacement:

$$\vec{\Delta}_{\rm lat}(x, y) = \frac{\vec{F}_{\rm lat}(x, y)}{k_{\rm CO}}, \tag{2}$$

where $k_{\rm CO}$ is the lateral spring constant of the CO tip. The constant $k_{\rm CO}$ is an adjustable empirical parameter which is set to be different values in our simulations (see Ref. [64] S1 for more computational details).

Using these theoretical tools, we simulate the images of the molecular species of interest. For pentacene, we relax the molecule on the Cu (111) surface starting from an adsorption geometry proposed by Toyoda *et al.* [65]. The sideview in Fig. 2(a) illustrates the bending of the planar pentacene molecule on the Cu substrate. The terminal rings move

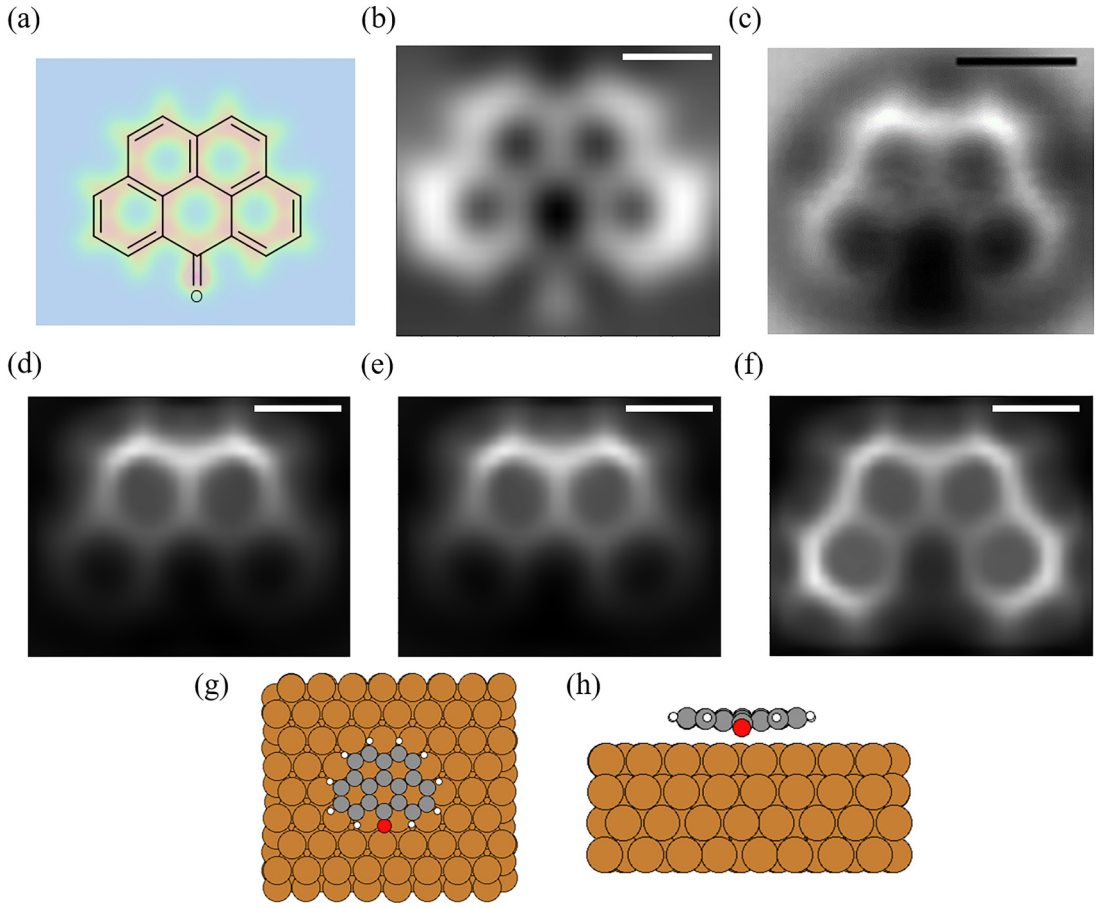

FIG. 3. (a) Kekulé structure overlaps with the charge density map (red-blue-green scale) at a plane that is 1.2 a.u. above the planar naphthanthrone molecule. (b) Simulated nc-AFM image of the planar Naphthanthrone molecule before structural relaxation on a Cu (111) substrate, tip height = 5.4 a.u., tip tilting correction not applied. (c) Experimental nc-AFM image of naphthanthrone on a Cu (111) surface. [(d)–(f)] Simulated nc-AFM images of naphthanthrone molecule on Cu (111) at (d) fcc30°, (e) hcp30°, and (f) atop30° adsorption sites. $k_{CO} = 0.80\,\mathrm{N/m}$. [(g) and (h)] Top and side views of the relaxed naphthanthrone molecule on a four-layered Cu (111) surface at the atop30° adsorption site. Brown: Cu, gray: C, red: O, white: H. The scale bars correspond to 9.45 a.u. in (c) and correspond to 5 a.u. in (b) and (d)–(f), respectively. (c) is adapted from Ref. [67].

upward relative to the molecular center. The molecule also experiences a slight tilt perpendicular to the long axis. Our relaxed structure agrees with previous theoretical work [66]. This structural relaxation significantly improves the quality and accuracy of the simulation in terms of the size of the rings and the edges as illustrated in Figs. 2(b) and 2(c). For example, the brightness of the terminating edges is enhanced by the bent structure. In addition, the slight tilt of the molecule on the Cu substrate introduces the asymmetry along the long axis in the simulated image. These features agree well with the corresponding ones in the experimental image shown in Fig. 2(d).

For naphthanthrone, we first perform AFM calculations assuming a planar geometry illustrated in Figs. 3(a) and 3(b), which does not agree with the experimental image [Fig. 3(c)] as the C = O bond is visible in our simulation [Fig. 3(b)]. We find the charge density of the C = O bond (at a plane 1.2 a.u. above the molecule) matches that of the carbon-carbon covalent bonds [Fig. 3(a)]. Typically, a higher charge density correlates with a brighter spot in a nc-AFM image. However, the C = O bond is not observed in experiment as illustrated in Fig. 3(c).

To account for the absence of the C = O bond in the experimental image, we consider possible interaction between the specimen and the Cu substrate. We structurally relax the naphthanthrone molecule at two adsorption sites: (1) fcc30° and (2) hcp30° which are the experimentally determined adsorption sites in Ref. [67]. We take the center carbon ring as the reference ring and use the nomenclature for adsorption sites as illustrated in Fig. 1 of Ref. [68]. At each site, we compute the total energy of the system as a function of the adsorption distance while keeping the initial relaxed molecular structure fixed. We obtain an approximate adsorption distance of the naphthanthrone molecule by minimizing the total energy. We then perform full structural relaxation calculations at each site starting from the corresponding estimated adsorption distance. Relaxation at both adsorption sites leads to tilted and bent structures where the O atom pointing toward the Cu surface (see Ref. [64] S2 for the atomic coordinates of the relaxed systems). The calculated bent structure agrees with a previous study on a similar O-containing organic molecule adsorbed on a Cu (111) surface [69].

Figures 3(d) and 3(e) show the simulated nc-AFM images of the relaxed naphthanthrone molecule at fcc30° and hcp30°

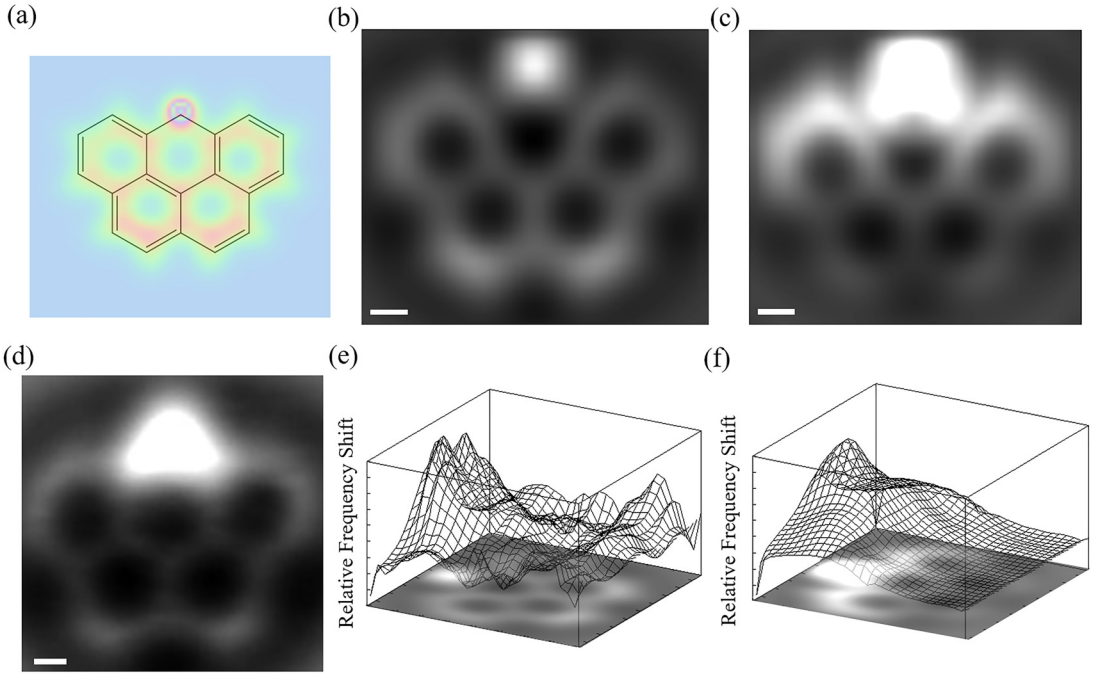

FIG. 4. (a) Kekulé structure overlaps with the charge density map (red-blue-green scale) at a plane that is 1.8 a.u. above the planar olympicene molecule. [(b) and (c)] Simulated nc-AFM images of (b) planar and (c) tilted (by approximately 4° where the $-CH_2$ end points opposite to the substrate) specimen, tip height = 6.0 a.u., $k_{CO} = 0.90\,N/m$. (d) Experimental nc-AFM image of olympicene on a Cu (111) surface. (e) and (f) are 3D profiles of the corresponding relative frequency shift values of (b) and (c). The scale bars correspond to 2 a.u. in (b) and (c) and correspond to 1.89 a.u. in (d). (d) is adapted from Ref. [67].

sites respectively. Our simulation successfully replicates the absence of the C = O bond in the nc-AFM image, owing to the attraction between the O atom and the Cu substrate. Although the essential features of the experimental image are reproduced, the two bottom carbon rings are partially visible.

In the structural relaxation of naphthanthrone, we noted that the O atom has a tendency to move toward the nearest fcc hollow site. Based on this observation, we examined another adsorption site, atop30° (see Fig. 1 in Ref. [68] for nomenclature), by placing the O atom on an fcc hollow site. We obtain a similar, but less tilted, structure as shown in Figs. 3(g) and 3(h) after relaxation. The resulting simulated image [Fig. 3(f)] yields a better agreement with the experimental image as not only the C = O bond disappears but also the edges of the four carbon rings are brighter and better defined. One possible approach to imaging the C = O bond experimentally is to use a more chemically inactive substrate such as a bilayer NaCl (100) or a Xe (111) substrates [70].

The experimental nc-AFM image of olympicene [Fig. 4(d)] shows an interesting triangular bright feature for the $-CH_2$ group. We calculate the charge density above the sp^3 hybridized carbon atoms at a plane 1.8 a.u. above the $-CH_2$ group. We find that the density is notably higher than the rest of the carbon atoms as one of the attached H atoms points toward the tip. This $-CH_2$ group appears as a bright circular spot rather than a triangular area in the corresponding simulated nc-AFM image as shown in Fig. 4(b). A similar issue with respect to H atom near the tip is discussed in Refs. [25,33].

We rotate the specimen by an empirical adjusted tilt angle of approximately 4°, which is similar to the tilt angle in

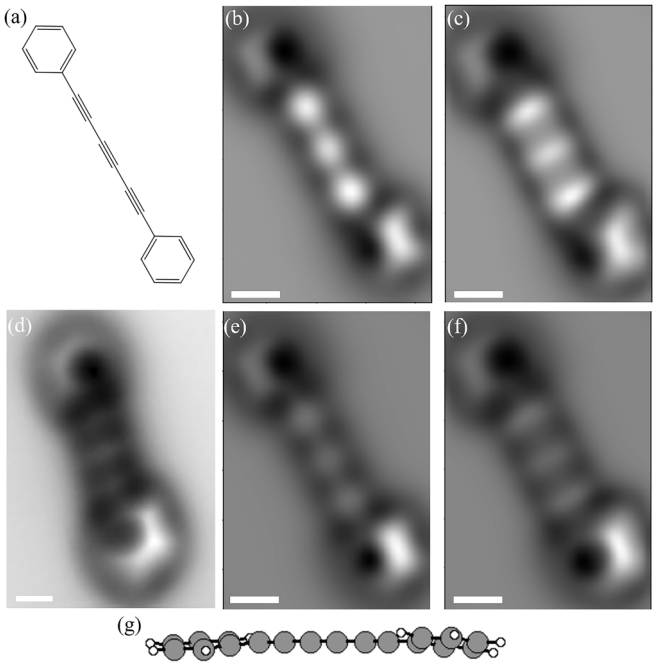

FIG. 5. (a) Kekulé structure of PHTB. [(b), (c), (e), and (f)] Simulated nc-AFM image of PHTB before and after moving the triple bond away from the tip. Tip height is 6.6 a.u. [(b) and (e)] No tip tilting correction applied. [(c) and (f)] Tip tilting correction applied with the lateral spring constant $k_{CO} = 0.40\,N/m$. (d) Experimental nc-AFM image of PHTB on bilayer NaCl on a Cu(111) surface. (g) Side view of the relaxed PHTB molecule. Gray: C, white: H. The scale bars correspond to 5 a.u. (d) is adapted from Ref. [24]. (b) and (c) are from Ref. [34].

Ref. [71] (the $-CH_2$ end points opposite to the substrate), to investigate the steric effect on the simulated nc-AFM images. Figure 4(c) shows that the shape of the bright spot is much improved to experiment when compared with the planar molecule. Figures 4(e) and 4(f) respectively illustrate the 3D profiles of relative frequency shift values of the planar and the tilted olympicene molecule generated with a CO-functionalized tip. We find that the planar specimen generates isolated Δf peaks while the tilted geometry washes out the peaks. This supports a conjecture that the true angle is between 0° and 4° (based on the size of the triangular area) when placing on a Cu (111) surface peaks while the tilted geometry washes out the peaks. This supports a conjecture that the true angle is between 0° and 4° (based on the size of the triangular area) when placing on a Cu (111) surface.

With respect to the PHTB molecule, there are two key features: (1) the triple bonds appear to be fainter than the singe/double bonds; (2) the benzene rings appear to be defective where only about half of the rings are imaged. We manually adjust the twisted angles of the two benzene rings to match the simulated image with the experiment as illustrated in Fig. 5. We find the triple bonds appear to be fainter when they are moved away from the tip. The adjusted twisted geometry appears more accurate than previous work [Figs. 5(b) and 5(c)] [34]. When the tip relaxation is considered [Figs. 5(c) and 5(f)], the appearance of the triple bonds changes from spheroidal to ellipsoidal. Fig. 5(g) shows a side view of the twisted structure of PHTB which corresponds to the simulated images. The twisted benzene rings offer an explanation of the two defective rings in the nc-AFM images. In addition, since this experiment was performed on bilayer NaCl which is a chemically inactive substrate, we expect the interaction between the specimen and the substrate can be neglected. The weak interaction is demonstrated by the manual adjustments of the molecular structure. We treat the substrate as a flat inert surface. The two terminal benzene rings support the middle carbon chain. This interpretation helps to explain the invisible triple bonds in larger long-chain organic molecules [72].

We study four benchmark molecules to reveal the chemical and steric effects on nc-AFM images through quantum simulations in real space. For pentacene and naphthanthrone, we find relaxing the molecules on the substrate significantly improves the accuracy of the nc-AFM simulation. In particular, we note that the absence of the C = O bond in nc-AFM naphthanthrone images can be ascribed to the bent structure of the molecule and the strong attraction between the O atom and the Cu substrate. For olympicene, we find that the tilting angle of the molecule has a direct impact on a bright triangular feature of the $-CH_2$ group. For PHTB, we find that the twisted nature leads to a fainter triple bond feature and a defective benzene ring feature. Our work provides a theoretical basis for interpreting nc-AFM images for nonplanar molecules.

The authors acknowledge support from the Welch Foundation under grant F-1837 and the U.S. Department of Energy under DOE/DE-FG02-06ER46286. The National Energy Research Scientific Computing (NERSC) and the Texas Advanced Computing Center (TACC) provided computational resources.

[1] G. Binnig, C. F. Quate, and C. Gerber, Atomic Force Microscope, Phys. Rev. Lett. **56**, 930 (1986).

[2] S. P. Jarvis, Resolving intra- and intermolecular structure with non-contact atomic force microscopy, Int. J. Mol. Sci. **16**, 19936 (2015).

[3] L. Gross, B. Schuler, N. Pavliček, S. Fatayer, Z. Majzik, N. Moll, D. Peña, and G. Meyer, Atomic force microscopy for molecular structure elucidation, Angew. Chem. Int. Ed. **57**, 3888 (2018).

[4] F. J. Giessibl, The qPlus sensor, a powerful core for the atomic force microscope, Rev. Sci. Instrum. **90**, 011101 (2019).

[5] J. R. Chelikowsky, D. Fan, A. J. Lee, and Y. Sakai, Simulating atomic force microscopy images, Phys. Rev. Mater. **3**, 110302 (2019).

[6] L. Gross, F. Mohn, N. Moll, P. Liljeroth, and G. Meyer, The chemical structure of a molecule resolved by atomic force microscopy, Science **325**, 1110 (2009).

[7] L. Gross, Recent advances in submolecular resolution with scanning probe microscopy, Nat. Chem. **3**, 273 (2011).

[8] L. Gross, F. Mohn, N. Moll, B. Schuler, A. Criado, E. Guitián, D. Peña, A. Gourdon, and G. Meyer, Bond-order discrimination by atomic force microscopy, Science **337**, 1326 (2012).

[9] M. P. Boneschanscher, J. van der Lit, Z. Sun, I. Swart, P. Liljeroth, and D. Vanmaekelbergh, Quantitative atomic resolution force imaging on epitaxial graphene with reactive and nonreactive AFM probes, ACS Nano. **6**, 10216 (2012).

[10] D. G. de Oteyza, P. Gorman, Y.-C. Chen, S. Wickenburg, A. Riss, D. J. Mowbray, G. Etkin, Z. Pedramrazi, H.-Z. Tsai, A. Rubio, M. F. Crommie, and F. R. Fischer, Direct imaging of covalent bond structure in single-molecule chemical reactions, Science **340**, 1434 (2013).

[11] J. Zhang, P. Chen, B. Yuan, W. Ji, Z. Cheng, and X. Qiu, Real-space identification of intermolecular bonding with atomic force microscopy, Science **342**, 611 (2013).

[12] J. van der Lit, M. P. Boneschanscher, D. Vanmaekelbergh, M. Ijäs, A. Uppstu, M. Ervasti, A. Harju, P. Liljeroth, and I. Swart, Suppression of electron-vibron coupling in graphene nanoribbons contacted via a single atom, Nat. Commun. **4**, 2023 (2013).

[13] A. Riss, S. Wickenburg, P. Gorman, L. Z. Tan, H.-Z. Tsai, D. G. de Oteyza, Y.-C. Chen, A. J. Bradley, M. M. Ugeda, G. Etkin, S. G. Louie, F. R. Fischer, and M. F. Crommie, Local electronic and chemical structure of Oligo-acetylene derivatives formed through radical cyclizations at a surface, Nano Lett. **14**, 2251 (2014).

[14] M. Schneiderbauer, M. Emmrich, A. J. Weymouth, and F. J. Giessibl, CO Tip Functionalization Inverts Atomic Force Microscopy Contrast via Short-range Electrostatic Forces, Phys. Rev. Lett. **112**, 166102 (2014).

[15] S. K. Hämäläinen, N. van der Heijden, J. van der Lit, S. den Hartog, P. Liljeroth, and I. Swart, Intermolecular Contrast in Atomic Force Microscopy Images without Intermolecular Bonds, Phys. Rev. Lett. **113**, 186102 (2014).

[16] H. Sang, S. P. Jarvis, Z. Zhou, P. Sharp, P. Moriarty, J. Wang, Y. Wang, and L. Kantorovich, Identifying tips for intramolecular NC-AFM imaging via in situ fingerprinting, Sci. Rep. **4**, 6678 (2014).

[17] M. Emmrich, F. Huber, F. Pielmeier, J. Welker, T. Hofmann, M. Schneiderbauer, D. Meuer, S. Polesya, S. Mankovsky, D. Ködderitzsch, H. Ebert, and F. J. Giessibl, Subatomic resolution force microscopy reveals internal structure and adsorption sites of small iron clusters, Science **348** 308 (2015).

[18] E. I. Altman, M. Z. Baykara, and U. D. Schwarz, Noncontact atomic force microscopy: An emerging tool for fundamental catalysis research, Acc. Chem. Res. **48**, 2640 (2015).

[19] H. Z. Tsai, A. A. Omrani, S. Coh, H. Oh, S. Wickenburg, Y. W. Son, D. Wong, A. Riss, H. S. Jung, G. D. Nguyen, G. F. Rodgers, A. S. Aikawa, T. Taniguchi, K. Watanabe, A. Zettl, S. G. Louie, J. Lu, M. L. Cohen, and M. F. Crommie, Molecular self-assembly in a poorly screened environment: F_4TCNQ on graphene/BN, ACS Nano **9**, 12, 12168 (2015).

[20] A. Sánchez-Grande, B. De la Torre, J. Santos, B. Cirera, K. Lauwaet, T. Chutora, S. Edalatmanesh, P. Mutombo, J. Rosen, R. Zbořil, R. Miranda, J. Björk, P. Jelínek, N. Martín, and D. Écija, On-surface synthesis of ethynylene-bridged anthracene polymers, Angew. Chem. Int. Ed. **58**, 6559 (2019).

[21] B. Schuler, S. Fatayer, G. Meyer, E. Rogel, M. Moir, Y. Zhang, M. R. Harper, A. E. Pomerantz, K. D. Bake, M. Witt, D. Peña, J. D. Kushnerick, O. C. Mullins, C. Ovalles, F. G. A. van den Berg, and L. Gross, Heavy Oil Based Mixtures of Different Origins and Treatments Studied by Atomic Force Microscopy, Energy Fuels **31**, 6856 (2017).

[22] Y. Zhang, Nonalternant Aromaticity and Partial Double Bond in Petroleum Molecules Revealed: Theoretical Understanding of Polycyclic Aromatic Hydrocarbons Obtained by Non-contact Atomic Force Microscopy, Energy Fuels **33**, 3816 (2018).

[23] Y. Cao, J. Qi, Y. F. Zhang, L. Huang, Q. Zheng, X. Lin, Z. Cheng, Y. Y. Zhang, X. Feng, S. X. Du, S. T. Pantelides, and H. J. Gao, Tuning the morphology of chevron-type graphene nanoribbons by choice of annealing temperature, Nano. Res. **11**, 6190 (2018).

[24] N. Pavliček, P. Gawel, D. R. Kohn, Z. Majzik, Y. Xiong, G. Meyer, H. L. Anderson, and L. Gross, Polyyne formation via skeletal rearrangement induced by atomic manipulation, Nature Chem. **10**, 853 (2018).

[25] J. Peng, J. Guo, P. Hapala, D. Cao, R. Ma, B. Cheng, L. Xu, M. Ondráček, P. Jelínek, E. Wang, and Y. Jiang, Weakly perturbative imaging of interfacial water with submolecular resolution by atomic force microscopy, Nat. Commun. **9**, 122 (2018).

[26] S. Fatayer, N. B. Poddar, S. Quiroga, F. Schulz, B. Schuler, S. V. Kalpathy, G. Meyer, D. Pérez, E. Guitián, D. Peña, W. J. Wornat, and L. Gross, Atomic force microscopy identifying fuel pyrolysis products and directing the synthesis of analytical standards, J. Am. Chem. Soc. **140**, 8156 (2018).

[27] A. Shiotari, Y. Sugimoto, and H. Kamio, Characterization of two- and one-dimensional water networks on Ni(111) via atomic force microscopy, Phys. Rev. Mater. **3**, 093001(R) (2019).

[28] D. Cao, Y. Song, J. Peng, R. Ma, J. Guo, J. Chen, X. Li, Y. Jiang, E. Wang, and L. Xu, Advances in atomic force microscopy: weakly perturbative imaging of the interfacial water, Front. Chem. **7**, 626 (2019).

[29] S. Fatayer, F. Albrecht, Y. Zhang, D. Urbonas, D. Peña, N. Moll, and L. Gross, Molecular structure elucidation with charge-state control, Science **365**, 142 (2019).

[30] Y. Zhang, F. Schulz, B. Rytting, C. Walters, K. Kaiser, J. Metz, M. Harper, S. Merchant, A. Mennito, K. Qian, J. Kushnerick, P. Kilpatrick, and L. Gross, Elucidating the Geometric Substitution of Petroporphyrins by Spectroscopic Analysis and AFM Molecular Imaging. Energy Fuels **33**, 6088 (2019).

[31] K. Kaiser, L. M. Seriven, F. Schulz, P. Gawel, L. Gross, and H. L. Anderson, An sp-hybridized molecular carbon allotrope, cyclo[18]carbon, Science **365**, 1299 (2019).

[32] H. F. Wen, Q. Zhang, Y. Adachi, M. Miyazaki, Y. Sugawara, and Y. J. Li, Contrast inversion of O adatom on rutile TiO_2(110)-(1×1) surface by atomic force microscopy imaging, Appl. Surf. Sci. **505**, 144623 (2020).

[33] S. Kawai, O. Krejčí, A. S. Foster, R. Pawlak, F. Xu, L. Peng, A. Orita, and E. Meyer, Diacetylene linked anthracene oligomers synthesized by one-shot homocoupling of trimethylsilyl on Cu(111), ACS. Nano. **12**, 8791 (2018).

[34] D. Fan, Y. Sakai, and J. R. Chelikowsky, Discrimination of bond order in organic molecules using noncontact atomic force microscopy, Nano Lett. **19**, 5562 (2019).

[35] D. Fan, Y. Sakai, and J. R. Chelikowsky, Real-space pseudopotential calculations for simulating noncontact atomic force microscopy images, J. Vac. Sci. Tech. B. **36**, 04H102 (2018).

[36] A. J. Lee, Y. Sakai, and J. R. Chelikowsky, Simulating contrast inversion in atomic force microscopy imaging with real-space pseudopotentials, Phys. Rev. B **95**, 081401(R) (2017).

[37] Y. Sakai, A. J. Lee, and J. R. Chelikowsky, First-principles atomic force microscopy image simulations with density embedding theory, Nano Lett.**16**, 3242 (2016).

[38] A. J. Lee, Y. Sakai, M. Kim, and J. R. Chelikowsky, Repulsive tip tilting as the dominant mechanism for hydrogen bond-like features in atomic force microscopy imaging, Appl. Phys. Lett. **108**, 193102 (2016).

[39] M. Kim and J. R. Chelikowsky, CO tip functionalization in subatomic resolution atomic force microscopy, Appl. Phys. Lett. **107**, 163109 (2015).

[40] M. Kim and J. R. Chelikowsky, Simulated non-contact atomic force microscopy for GaAs surfaces based on real-space pseudopotentials, Appl. Surf. Sci. **303**, 163 (2014).

[41] T.-L. Chan, C. Z. Wang, K. M. Ho, and J. R. Chelikowsky. Efficient First-Principles Simulation of Noncontact Atomic Force Microscopy, Phys. Rev. Lett. **102**, 176101 (2009).

[42] M. Ellner, P. Pou, and R. Pérez, Molecular identification, bond order discrimination, and apparent intermolecular features in atomic force microscopy studied with a charge density based method, ACS Nano **13**, 786 (2019).

[43] X. Hu, P. Egberts, Y. Dong, and A. Martini, Molecular dynamics simulation of amplitude modulation atomic force microscopy, Nanotechnology **26**, 235705 (2015).

[44] D. Z. Gao, J. Grenz, M. B. Watkins, F. Federici Canova, A. Schwarz, R. Wiesendanger, and A. L. Shluger, Using metallic noncontact atomic force microscope tips for imaging

insulators and polar molecules: Tip characterization and imaging mechanisms, ACS Nano **8**, 5339 (2014).
[45] P. Hapala, G. Kichin, C. Wagner, F. S. Tautz, R. Temirov, and P. Jelinek, Mechanism of high-resolution STM/AFM imaging with functionalized tips, Phys. Rev. B **90**, 085421 (2014).
[46] F. Federici Canova, A. S. Foster, M. K. Rasmussen, K. Meinander, F. Besenbacher, and J. V. Lauristen, Non-contact atomic force microscopy study of hydroxyl groups on the spinel $MgAl_2O_4$(100) surface, Nanotechnology **23**, 325703 (2012).
[47] V. Caciuc and H. Hölscher, Ab initio simulation of atomic-scale imaging in noncontact atomic force microscopy, Nanotechnology **20**, 264006 (2009).
[48] P. Hohenberg and W. Kohn, Inhomogeneous electron gas, Phys. Rev. **136**, B864 (1964).
[49] W. Kohn and L. J. Sham, Self-consistent equations including exchange and correlation effects, Phys. Rev. **140**, A1133 (1965).
[50] J. R. Chelikowsky, N. Troullier, and Y. Saad, Finite-Difference-Pseudopotential Method: Electronic Structure Calculations without a Basis, Phys. Rev. Lett. **72**, 1240 (1994).
[51] J. R. Chelikowsky, The pseudopotential-density functional method applied to nanostructures, J. Phys. D: Appl. Phys. **33**, R33 (2000).
[52] M. M. G. Alemany, M. Jain, L. Kronik, and J. R. Chelikowsky, Real-space pseudopotential method for computing the electronic properties of periodic system, Phys. Rev. B **69**, 075101 (2004).
[53] L. Kronik, A. Makmal, M. L. Tiago, M. M. G. Alemany, M. Jain, X. Huang, Y. Saad, and J. R. Chelikowsky, PARSEC-the pseudopotential algorithm for real-space electronic structure calculations: Recent advances and novel applications to nanostructures, Phys. Status Solidi B **243**, 1063 (2006).
[54] Y. Saad, J. R. Chelikowsky, and S. M. Shontz. Numerical methods for electronic structure calculations of materials, SIAM Rev. **52**, 3 (2010).
[55] A. Natan, A. Benjamini, D. Naveh, L. Kronik, M. L. Tiago, S. P. Beckman, and J. R. Chelikowsky, Real-space pseudopotential method for first principles calculations of general periodic and partially periodic systems, Phys. Rev. B **78**, 075109 (2008).
[56] F. J. Giessibl, Forces and frequency shifts in atomic-resolution dynamic-force microscopy, Phys. Rev. B **56**, 16010 (1997).
[57] F. J. Giessibl, A direct method to calculate tip-sample forces from frequency shifts in frequency-modulation atomic force microscopy, Appl. Phys. Lett. **78**, 123 (2001).
[58] N. Troullier and J. L. Martins, Efficient pseudopotentials for plane-wave calculations, Phys. Rev. B **43**, 1993 (1991).
[59] D. M. Ceperley and B. J. Alder, Ground State of the Electron Gas by a Stochastic Method, Phys. Rev. Lett. **45**, 566 (1980).
[60] J. P. Perdew and A. Zunger, Self-interaction correction to density-functional approximations for many-electron systems, Phys. Rev. B **23**, 5048 (1981).
[61] T. A. Wesołowski, S. Shedge, and X. Zhou, Frozen-density embedding strategy for multilevel simulations of electronic structure, Chem. Rev. **115**, 5891 (2015).
[62] C.-S. Guo, M. A. Van Hove, X. Ren, and Y. Zhao, High-resolution model for noncontact atomic force microscopy with a flexible molecule on the tip apex, J. Phys. Chem. C **119**, 1483 (2015).
[63] C.-S. Guo, X. Xin, M. A. Van Hove, X. Ren, and Y. Zhao, Origin of the contrast interpreted as intermolecular and intramolecular bonds in atomic force microscopy image, J. Phys. Chem. C **119**, 14195 (2015).
[64] See Supplemental Material at http://link.aps.org/supplemental/10.1103/PhysRevMaterials.4.053802 for parameters of AFM calculations for the specimens and the relaxed atomic coordinates for pentacene and naphthanthrone on Cu (111).
[65] K. Toyoda, I. Hamada, K. Lee, S. Yanagisawa, and Y. Morikawa, Density functional theoretical study of pentacene/noble metal interfaces with van der Waals corrections: Vacuum level shifts and electronic structures, J. Chem. Phys. **132**, 134703 (2010).
[66] B. Schuler, W. Liu, A. Tkatchenko, N. Moll, G. Meyer, A. Mistry, D. Fox, and L. Gross, Adsorption Geometry Determination of Single Molecules by Atomic Force Microscopy, Phys. Rev. Lett. **111**, 106103 (2013).
[67] A. Mistry, B. Moreton, B. Schuler, F. Mohn, G. Meyer, L. Gross, A. Williams, P. Scott, G. Costantini, and D. J. Fox, The synthesis and STM/AFM imaging of 'olympicene' benzo[*cd*]pyrenes, Chem. Eur. J. **21**, 2011 (2015).
[68] W. Liu, V. G. Ruiz, G. X. Zhang, B. Santra, X. Ren, M. Scheffler, and A. Tkatchenko, Structure and energetics of benzene adsorbed on transition-metal surfaces: density-functional theory with van der Waals interactions including collective substrate response, New J. Phys. **15**, 053046 (2013).
[69] N. J. van der Heijden, P. Hapala, J. A. Rombouts, J. van der Lit, D. Smith, P. Mutombo, M. Švec, P. Jelinek, and I. Swart, Characteristic contrast in Δf_{min} maps of organic molecules using atomic force microscopy, ACS Nano **10**, 8517 (2016).
[70] N. Pavliček, A. Mistry, Z. Majzik, N. Moll, G. Meyer, D. J. Fox, and L. Gross, Synthesis and characterization of triangulene, Nat. Nanotech. **12**, 308 (2017).
[71] P. Zahl and Y. Zhang, Guide for atomic force microscopy image analysis to discriminate heteroatoms in aromatic molecules, Energy Fuels **33**, 4775 (2019).
[72] B. Schuler, Y. Zhang, S. Collazos, S. Fatayer, G. Meyer, D. Pérez, E. Guitián, M. R. Harper, J. D. Kushnerick, D. Peña, and L. Gross, Characterizing aliphatic moieties in hydrocarbons with atomic force microscopy, Chem. Sci. **8**, 2315 (2017).

Correction: Equation (2) contained a minor error and has been fixed.